Supplementary Information for *Multiscale integration of environmental stimuli in plant tropism produces complex behavior*

Derek E. Moulton, Hadrien Oliveri, and Alain Goriely

Mathematical Institute, University of Oxford, Oxford OX2 6GG, United Kingdom

1. Rod geometry and Kirchhoff equations

The morphology of the plant is determined by solving the Kirchhoff equations for an elastic rod with non-zero evolving intrinsic curvature and axial growth. Here we briefly recall the basic elements of Cosserat rod theory. A *rod* is a space curve $\mathbf{r}(S) \in \mathbb{R}^3$, known as the *centerline*, equipped with two additional unit orthonormal vector fields $(\mathbf{d}_1(S), \mathbf{d}_2(S))$ representing the orientation of a cross section at S. The *general frame* is obtained by defining $\mathbf{d}_3(S) = \mathbf{d}_1(S) \times \mathbf{d}_2(S)$ and we note that $\{\mathbf{d_1}, \mathbf{d_2}, \mathbf{d_3}\}$ forms a right-handed orthonormal basis. The components of a vector $\mathbf{a} = \mathsf{a}_1\mathbf{d}_1 + \mathsf{a}_2\mathbf{d}_2 + \mathsf{a}_3\mathbf{d}_3$ in the local basis are denoted by $\mathbf{a} = (\mathsf{a}_1, \mathsf{a}_2, \mathsf{a}_3)$. We note that $|\mathbf{a}| = |\mathbf{a}|$.

We choose the material parameter s to be the current arc length, i.e. in the grown configuration, and S to be the material arc length in an initial pre-grown configuration. These are related by the growth stretch

$$\gamma := \frac{\partial s}{\partial S}. \tag{1}$$

For an unshearable rod, we may choose $\mathbf{d}_3$ to align with the tangent direction, so that

$$\frac{\partial \mathbf{r}}{\partial s} = \mathbf{d}_3, \tag{2}$$

or equivalently

$$\frac{\partial \mathbf{r}}{\partial S} = \gamma\mathbf{d}_3. \tag{3}$$

A complete kinematic description of the frame is given by:

$$\frac{\partial \mathbf{d}_i}{\partial s} = \mathbf{u} \times \mathbf{d}_i, \quad i = 1, 2, 3, \tag{4}$$

where $\mathbf{u}$ is the *Darboux vector*. The first two components $(\mathsf{u}_1, \mathsf{u}_2)$ of the Darboux vector are associated with the Frenet curvature while u_3 represents twisting, that is the rotation of the basis (not the curve) around the $\mathbf{d}_3$ vector. It contains both information on the Frenet torsion τ of the centerline and on the rotation of the cross section for increasing values of s.

In particular, if the rod is assumed to be inextensible, the Darboux vector is related to the usual notion of Frenet curvature and torsion κ and τ by

$$\cot\varphi = \frac{\mathsf{u}_2}{\mathsf{u}_1}, \tag{5}$$

$$\kappa = \sqrt{\mathsf{u}_1^2 + \mathsf{u}_2^2}, \tag{6}$$

$$\tau = \mathsf{u}_3 + \frac{\mathsf{u}_2'\mathsf{u}_1 - \mathsf{u}_1'\mathsf{u}_2}{\mathsf{u}_1^2 + \mathsf{u}_2^2}. \tag{7}$$

where prime denotes differentiation with respect to current arc length s. Also, φ is the angle between the normal and the vector $\mathbf{d}_1$. The quantity $\partial\varphi/\partial s$, *the excess twist*, represents the rotation of the local basis with respect to the Frenet frame as the arc length increases.

The stress on the cross section at $\mathbf{r}(s)$ from adjacent segments with larger material coordinates ($s' > s$) gives rise to a *resultant force* $\mathbf{n}(s)$ and *resultant couple* $\mathbf{m}(s)$. These satisfy the balance of linear and angular momentum, which in mechanical equilibrium read:

$$\frac{\partial \mathbf{n}}{\partial s} + \mathbf{f} = \mathbf{0}, \tag{8}$$

$$\frac{\partial \mathbf{m}}{\partial s} + \frac{\partial \mathbf{r}}{\partial s} \times \mathbf{n} = \mathbf{0}. \tag{9}$$

Here $\mathbf{f}$ is a linear force density accounting for any external forces acting on the rod, such as contact forces.

The system is closed by boundary conditions and constitutive laws. We restrict to an inextensible rod in this paper, and thus only a constitutive equation relating moment $\mathbf{m}$ to curvature is needed. For a quadratic elastic energy, this takes the general form $\mathbf{m} = \mathbf{K}(\mathbf{u} - \hat{\mathbf{u}})$, where $\mathbf{K}$ is a stiffness matrix. Considering the simplest and most widely used case of a diagonal $\mathbf{K}$, we have

$$\mathbf{m} = K_1(\mathsf{u}_1 - \hat{\mathsf{u}}_1)\mathbf{d}_1 + K_2(\mathsf{u}_2 - \hat{\mathsf{u}}_2)\mathbf{d}_2 + K_3(\mathsf{u}_3 - \hat{\mathsf{u}}_3)\mathbf{d}_3. \tag{10}$$

In this case, the Kirchhoff theory tells us that the stiffnesses are

$$K_1 = E\mathcal{I}_1, \quad K_2 = E\mathcal{I}_2, \quad K_3 = \mu J \tag{11}$$

where E is the Young's modulus, μ the second Lamé parameter and J, $\mathcal{I}_{1,2}$ depend on the cross-sectional shape (see main text).

In terms of boundary conditions, we primarily consider a plant that is held clamped at one end and free at the other. Denoting the clamped end $s = 0$, and the free end $s = \ell$, these amount to fixing the position and frame at $s = 0$:

$$\mathbf{r}(0, t) = \mathbf{r}_0, \quad \mathbf{d}_i(0, t) = \mathbf{d}_{i,0}, \quad i = 1, 2, 3, \tag{12}$$

and imposing zero force and moment at $s = \ell$:

$$\mathbf{m}(\ell, t) = \mathbf{n}(\ell, t) = \mathbf{0}. \tag{13}$$

As the elastic timescale is much shorter than the growth timescale, mechanical equilibrium is assumed at all times, and the intrinsic curvatures and growth stretch γ are updated in a quasi-static fashion via a simple forward Euler time-stepping of the appropriate evolution law.

2. From 3D growth field to 1D elasticity

In order to use the Kirchhoff equations described in the previous section, we need to obtain the intrinsic curvatures from the tropism models. These are obtained as solutions of evolution equations. Here, we follow the framework of (1) to obtained the intrinsic curvatures from a growth tensor defined on a 3D tubular structure. In this framework, we define the centerline as the curve passing through the centroids of each cross section so that

$$\int_{\Omega_S} x_1 \, \mathrm{d}x_1 \mathrm{d}x_2 = \int_{\Omega_S} x_2 \, \mathrm{d}x_1 \mathrm{d}x_2 = \int_{\Omega_S} x_1 x_2 \, \mathrm{d}x_1 \mathrm{d}x_2 = 0. \tag{14}$$

At any point in the material, the growth tensor can be written

$$\mathbf{G} = G_{ij}\mathbf{e}_i \otimes \mathbf{e}_j, \quad i, j = 1, 2, 3,$$

where in general each G_{ij} may be functions of position, and $(\mathbf{e}_1, \mathbf{e}_2, \mathbf{e}_3)$ are Cartesian basis vectors that are chosen to coincide with the frame $(\mathbf{d}_1, \mathbf{d}_2, \mathbf{d}_3)$ in the initial pre-deformed state of the plant.

⁶⁴ Conceptually, the components of $\mathbf{G}$ define the expansion (or contraction) of material both as a local
⁶⁵ property and as directional quantities. For example, if $G_{11} > 1$ then cells will expand in the $\mathbf{d}_1$ direction.
⁶⁶ The determinant of $\mathbf{G}$ describes the net gain or loss of mass at each point; here it is worthwhile to note
⁶⁷ that growth without a change of mass is possible, and it is also possible to have a growth field for which
⁶⁸ points gain or lose mass while the total mass for a cross section stays fixed.

⁶⁹ The quantity that is of most relevance for capturing a tropic growth response is the term G_{33}; this term
⁷⁰ describes axial elongation; it is the heterogeneity of this term across a section that generates curvature in
⁷¹ the plant. While other terms may play a role, for instance in changing the cross-sectional geometry, we
⁷² posit that this will typically be a secondary effect (for the general theory see (1)) and we assume the form

⁷³
$$\mathbf{G} = \mathrm{diag}(1, 1, 1 + g). \tag{15}$$

⁷⁴ For this growth tensor, the key result of (1) is that the intrinsic curvatures are given explicitly by

⁷⁵
$$\mathcal{I}_1 \hat{u}_1(S, t) = \int_{\Omega_S} x_2 g(x_1, x_2, S, t)\,\mathrm{d}x_1 \mathrm{d}x_2, \quad \mathcal{I}_2 \hat{u}_2(S, t) = -\int_{\Omega_S} x_1 g(x_1, x_2, S, t)\,\mathrm{d}x_1 \mathrm{d}x_2, \quad \hat{u}_3 = 0, \tag{16}$$

where

$$\mathcal{I}_1 := \int_{\Omega_S} x_2^2\,\mathrm{d}x_1 \mathrm{d}x_2, \quad \mathcal{I}_2 := \int_{\Omega_S} x_1^2\,\mathrm{d}x_1 \mathrm{d}x_2$$

⁷⁶ are the second moments of area. A straightforward extension of the derivation given in (1) shows that the
⁷⁷ axial elongation γ is given by

⁷⁸
$$\mathcal{A}\gamma = \int_{\Omega_S} g(x_1, x_2, S, t)\,\mathrm{d}x_1 \mathrm{d}x_2, \tag{17}$$

⁷⁹ where $\mathcal{A}$ is the cross-sectional area. Note in particular that if g is constant, then from Eq. (14) it follows
⁸⁰ that no curvature is generated, and the axial extension is equal to g; this reflects the simple and intuitive
⁸¹ notion that uniform axial growth does not create bending.

⁸² ## 3. Obtaining curvature and growth evolution laws

⁸³ As described in the main text, the axial growth g is connected to auxin concentration $A(x_1, x_2, s, t)$ by a
⁸⁴ growth law, assumed to have the form

⁸⁵
$$\frac{\partial g}{\partial t} = \beta(A - A^*). \tag{18}$$

⁸⁶ Since the shape of the cross sections is assumed to remain constant in time, we can take a time derivative
⁸⁷ across equations Eqs. (16) and (17) and utilize Eq. (18) to obtain evolution laws for the curvatures:

⁸⁸
$$\mathcal{I}_1 \frac{\partial \hat{u}_1}{\partial t} = \beta \int_{\Omega_S} x_2 A\,\mathrm{d}x_1 \mathrm{d}x_2, \quad \mathcal{I}_2 \frac{\partial \hat{u}_2}{\partial t} = -\beta \int_{\Omega_S} x_1 A\,\mathrm{d}x_1 \mathrm{d}x_2, \quad \frac{\partial \hat{u}_3}{\partial t} = 0. \tag{19}$$

⁸⁹ And similarly, the evolution law for the axial extension is

⁹⁰
$$\mathcal{A}\frac{\partial \gamma}{\partial t} = \beta \int_{\Omega_S} (A - A^*)\,\mathrm{d}x_1 \mathrm{d}x_2. \tag{20}$$

⁹¹ The approach outlined in (1) allows for more generic growth tensor $\mathbf{G}$, in which case the bending
⁹² stiffnesses about the $\mathbf{d}_1$ and $\mathbf{d}_2$ axes, as well as the torsional stiffness, can also change due to the growth.
⁹³ However, for the growth tensor (15), the stiffnesses are not impacted by g. Hence, for this modeling choice,
⁹⁴ when passing from tissue to organ scale, the tropic response is entirely encoded by the change in the intrinsic
⁹⁵ curvature of the plant as well as any axial extension.

⁹⁶ An extension of this model to include *autotropism* consists in adding a decay term

⁹⁷
$$\frac{\partial g}{\partial t} = \beta(A - A^*) - \xi(g - \overline{g}), \tag{21}$$

where

$$\overline{g} = \frac{1}{\mathcal{A}} \int_{\Omega_S} g \, \mathrm{d}x_1 \mathrm{d}x_2,$$

is the growth field average. The extra term $\xi(g - \overline{g})$ is the deviation of the growth field from its average value, thus providing a point-wise measure of the strain induced by differential growth. This term only impacts on the evolution laws for curvature, since it is differential growth that produces curvature. If, for instance, $g > 1$ is constant across the section, axial extension will occur without any curvature generation, and the autotropic term will not have an influence.

Specifically, note that the curvature evolution laws Eq. (19) become

$$\mathcal{I}_1 \frac{\partial \hat{u}_1}{\partial t} = \beta \int_{\Omega_S} x_2 A \, \mathrm{d}x_1 \mathrm{d}x_2 - \mathcal{I}_1 \xi u_1, \quad \mathcal{I}_2 \frac{\partial \hat{u}_2}{\partial t} = -\beta \int_{\Omega_S} x_1 A \, \mathrm{d}x_1 \mathrm{d}x_2 - \mathcal{I}_2 \xi u_2. \tag{22}$$

while the axial evolution law Eq. (20) is unchanged since

$$\int_{\Omega_S} (g - \overline{g}) \mathrm{d}x_1 \mathrm{d}x_2 = 0 \tag{23}$$

by definition of $\overline{g}$. In light of the form of Eqs. (19), (20) and (22), the objective for any given tropic stimulus is thus to obtain an expression for the terms

$$\int_{\Omega_S} x_2 A \, \mathrm{d}x_1 \mathrm{d}x_2, \quad \int_{\Omega_S} x_1 A \, \mathrm{d}x_1 \mathrm{d}x_2, \quad \int_{\Omega_S} A \, \mathrm{d}x_1 \mathrm{d}x_2 \tag{24}$$

via manipulation of the transport equation; given these, the evolution rules follow both with and without autotropism. We consider each tropism stimulus separately in the following section.

4. Specific curvature evolution laws

In this section we outline the steps to obtain the curvature evolution laws given in the main text from the assumptions on auxin transport and via the general evolution equations Eqs. (19) and (20). We first discuss estimates of the different components of the auxin transport equation, and then each tropism is considered in turn.

A. Comparing advection, diffusion, and turnover. One feature that is common to all evolution laws below is that we consider advection-dominated auxin transport, i.e. we restrict our attention to the zero-diffusion limit. To study the relative importance of advection and diffusion we compare the diffusive flux $\mathbf{J}^{\mathrm{diff}} = -D\nabla A$, where D is a diffusion coefficient, and an advective flux due to the environmental stimulus, which will generally take the form $\mathbf{J}^{\mathrm{stim}} = kA\mathbf{F}$, for a given auxin flow direction $\mathbf{F}$ (where $|\mathbf{F}| = 1$) and with flow rate k. Due to the nature of our tissue-level description of auxin transport, the parameters k and D are difficult to quantify directly. Indeed, at the cellular level, models of auxin transport (2) are highly dependent on cell geometry, and auxin flux may differ significantly in the cytoplasm compared to the apoplast, due to varying diffusivity. Additionally, the parameter k may be a proxy for multiple processes. For instance, in cell-based models of gravitropism, e.g. (3), the gravitational stimulus is modeled by modifying PIN efflux carrier locations on particular cells, based on the stem orientation with respect to gravity. In this approach, the flux $\mathbf{J}^{\mathrm{stim}}$ serves as a tissue-level proxy for a complex interaction of proteins and auxin transport both through and across cells; which cannot be easily related to a single parameter k. Moreover, this parameter is also related to the timescale of statoliths settling, e.g. (4).

To our knowledge, there is no well-established tissue-level auxin transport models and further experimental work, as well as explicit modeling connecting cell to tissue scales, is needed to identify these parameters. In the absence of such a theory, we can, nevertheless, justify the zero-diffusion limit $D = 0$ by estimating, in

the transport equation, the relative size of the diffusion and advection terms as follows:

$$\nabla \cdot \mathbf{J}^{\text{diff}} = D\nabla^2 A \sim [A]\frac{[D]}{[L]^2} \tag{25}$$

$$\nabla \cdot \mathbf{J}^{\text{stim}} = k\nabla \cdot (A\mathbf{F}) \sim [A]\frac{[k]}{[L]}, \tag{26}$$

where the symbol "$\sim$" denotes a scaling estimate and the bracket denotes the dimensions (e.g. L is the lengthscale of advection/diffusion so that [L] has the dimension of a length). To compare the relative size of these terms, note that in studies of the transport of an auxin pulse, auxin velocity has been measured to be on the order of $V \sim 1$ cm/hr $\approx 3 \cdot 10^{-4}$ cm/s (5), while the diffusion coefficient for auxin in aqueous solution has been estimated to be around $D \sim 10^{-6}$ cm^2/s (6) (and is presumed to be smaller in cytoplasm (5)). Note that L can vary significantly depending on the plant/organ under consideration, but for axial transport we have a typical L between 1 and 10 cm, while for cross-sectional transport we take $L \sim 0.1$ cm. For $L \sim 10$ cm we estimate

$$\nabla \cdot \mathbf{J}^{\text{diff}} \sim [A]10^{-8}\text{s}^{-1}, \quad \nabla \cdot \mathbf{J}^{\text{stim}} \sim [A]3 \cdot 10^{-5}\text{s}^{-1},$$

while for $L \sim 0.1$ cm, we have

$$\nabla \cdot \mathbf{J}^{\text{diff}} \sim [A]10^{-4}\text{s}^{-1}, \quad \nabla \cdot \mathbf{J}^{\text{stim}} \sim [A]3 \cdot 10^{-3}\text{s}^{-1}.$$

These estimates show that axial diffusion is negligible but that it may play a role in cross-sectional transport, though is still an order of magnitude smaller than might be expected from advection.

For the turnover modeled by the term $-QA$ in the transport equation, it is more difficult to obtain an estimate. However, in the case of an auxin source, the inclusion of turnover in the model enables to define a characteristic 'bending length' $l = U/Q$, which gives the distance from the source within which the tropic bending response occurs. Thus, we may estimate Q from the bending length and velocity. Taking $l \sim 1$ cm and with $U \sim 3 \cdot 10^{-4}$ cm/s, we obtain $Q = U/l \sim 3 \cdot 10^{-4}$ s^{-1}.

From a mathematical point of view, it is worth noting that in the cases of axial transport, the curvature evolution equations derived below can be obtained for zero turnover, and indeed would correspond to the derived forms in the well-defined limit of $Q \to 0$. The case of gravitropism is different in this regard, however, as gravitropism involves a cross-sectional auxin flow. The mathematical steps described below do not work in the case of zero turnover, i.e. $Q \to 0$ is a singular limit of the resulting gravitropic curvature evolution (which can be understood physically since, in the absence of turnover, auxin increases without bound).

Furthermore, it is worth highlighting that the limit case $D = 0$ enables for analytical tractability, and as shown below is key in establishing explicit curvature evolution laws. In the case of $D \neq 0$, the general model formulation remains valid, but the solution techniques applied below would not be directly applicable and may require a full computational approach to solving for auxin concentration.

B. Gravitropism. In the case of gravitropism, we consider a gravity driven auxin flux $\mathbf{J}^{\text{stim}} = kA\mathbf{f}$, where $\mathbf{f} := \mathsf{f}_1\mathbf{d}_1 + \mathsf{f}_2\mathbf{d}_2$ describes the cross-sectional component of the direction of gravity expressed in the local frame. The parameter k describes the gravitropic auxin flow rate. Since auxin transport timescales are generally smaller than the timescale associated with growth (7), and transport is only occurring on the short cross-sectional lengthscale, we also take the auxin concentration to be at steady state. Under these assumptions, the auxin concentration satisfies

$$\nabla \cdot (kA\mathbf{f}) = -QA + C_{\text{in}}\delta(r - r_0) - C_{\text{out}}\delta(x_1)\delta(x_2). \tag{27}$$

Here, the divergence is only taken in the cross-sectional variables (x_1, x_2), and Q is the turnover. The second and third terms on the right hand side account for a source C_{in} and sink C_{out} of auxin in each cross

section, providing a simple model of auxin transport routes. In particular, we consider here a source at radius $r = r_0$, which may for instance be taken to be near the cross-sectional radius in the case of epidermal auxin flow, and a sink at the center. These terms are needed simply to provide a source of auxin to be transported under gravity and stimulate growth; the specifics of these choices do not impact on the resulting equations.

Combining Eqs. (18), (19) and (27), and using Eq. (14), we obtain the following equation for the intrinsic curvature $\hat{u}_1$:

$$\mathcal{I}_1 \frac{\partial \hat{u}_1}{\partial t} = \beta \int_{\Omega_S} x_2 (A - A^*) \, dx_1 dx_2 = -\frac{\beta}{Q} \int_{\Omega_S} x_2 (\nabla \cdot kA\mathbf{f}) \, dx_1 dx_2. \tag{28}$$

Note that the source and sink terms both vanish on a circular cross section, as does the A^* term, assuming A^* is constant. This form for $\partial \hat{u}_1 / \partial t$ is not very useful, as it would still require solving for the auxin concentration at each time step. However, we may determine the evolution laws without explicitly solving for A, by noting the following identity

$$x_2 \nabla \cdot (kA\mathbf{f}) = \nabla \cdot (x_2 kA\mathbf{f}) - \nabla x_2 \cdot kA\mathbf{f} = \nabla \cdot (x_2 kA\mathbf{f}) - kA\mathsf{f}_2, \tag{29}$$

since $\nabla x_2 = \mathbf{d}_2$. Therefore, when integrating over the cross section, we have

$$\int_{\Omega_S} x_2 (\nabla \cdot kA\mathbf{f}) \, dx_1 dx_2 = \int_{\Omega_S} \nabla \cdot (x_2 kA\mathbf{f}) \, dx_1 dx_2 - k\mathsf{f}_2 \int_{\Omega_S} A \, dx_1 dx_2 = -k\mathsf{f}_2 \int_{\Omega_S} A \, dx_1 dx_2, \tag{30}$$

where we have used the divergence theorem and the no-flux boundary condition $\mathbf{J} \cdot \mathbf{n} = kA\mathbf{f} \cdot \mathbf{n} = \mathbf{0}$ on $\partial \Omega_S$ to write

$$\int_{\Omega_S} \nabla \cdot (x_2 kA\mathbf{f}) \, dx_1 dx_2 = \int_{\partial \Omega_S} x_2 kA\mathbf{f} \cdot \mathbf{n} \, ds = 0. \tag{31}$$

The problem is now reduced to evaluating an integral of only A over the cross section. We may again insert A via Eq. (27); the divergence term again vanishes by the no-flux boundary condition, while the delta function terms integrate to a constant $\Delta C = C_{\text{in}} - C_{\text{out}}$, i.e. the net auxin available in the cross section, so that

$$\int_{\Omega_S} x_2 (\nabla \cdot kA\mathbf{f}) \, dx_1 dx_2 = -\frac{k}{Q} \Delta C \mathsf{f}_2, \tag{32}$$

Combining the above, we obtain the relation provided in the main text:

$$\frac{\partial \hat{u}_1}{\partial t} = \mathcal{C}_{\text{grav}} \mathsf{f}_2, \tag{33}$$

where $\mathcal{C}_{\text{grav}} = \beta k \Delta C / (\mathcal{I}_1 Q^2)$. Similar steps lead to the evolution equations for $\hat{u}_2$ and γ as appearing in the main text:

$$\frac{\partial \hat{u}_2}{\partial t} = -\mathcal{C}_{\text{grav}} \mathsf{f}_1, \tag{34}$$

$$\frac{\partial \gamma}{\partial t} = \beta \left(\frac{\Delta C}{Q\mathcal{A}} - A^* \right). \tag{35}$$

Note that some plant organs align in a direction different to that of the gravitational field; the so-called gravitational setpoint angle (GSA) is often observed in branches of higher plants (8). in such branches, there exists an auxin-dependent 'antigravitropic' offset mechanism, effectively countering partially the growth response of auxin due to statolith settling under gravity (9). This mechanism can be easily included in our framework by altering the local gravitational field $\mathbf{f}$ to include the combined (and weighted) gravitational field and 'antigravitational' field, i.e. $\mathbf{f}$ would point in the direction of the GSA; however a full treatment of the problem likely would require consideration of the signaling pathways in the antigravitropic offset as shown in (9).

C. Phototropism. In the case of phototropism, we consider the following axial auxin transport equation

$$\frac{\partial A}{\partial t} - \frac{\partial}{\partial s}\left(UA\right) = -QA, \tag{36}$$

and with an auxin source at the tip $s = \ell$ given by:

$$A_{\text{tip}}(x_1, x_2, t) = -\kappa I(t)\left(\mathsf{e}_1(t)x_1 + \mathsf{e}_2(t)x_2\right) \tag{37}$$

where e is a unit vector pointing from the tip to the light source, I characterizes the intensity of the light, and κ characterizes the strength of the response to generate auxin. The fact that light induces an auxin gradient in the phototropic response is well established (10) and, in the absence of supplementary evidence, the simplest modeling choice is to assume that this gradient is linear. An exact solution to Eqs. (36) and (37) is given by

$$A(x_1, x_2, s, t) = A_{\text{tip}}\left(x_1, x_2, t - \frac{\ell - s}{U}\right)\exp\left(-\frac{Q(\ell - s)}{U}\right). \tag{38}$$

Following Eq. (19), we multiply by x_2 and integrate over a cross section. Since Eq. (37) gives A as a linear function of x_1, x_2, then using Eq. (14), we obtain the curvature evolution given in the main text:

$$\frac{\partial \hat{\mathsf{u}}_1}{\partial t} = -\mathcal{C}_{\text{photo}}\exp\left(-\frac{Q(\ell - s)}{U}\right)\mathsf{e}_2\left(t - \frac{\ell - s}{U}\right), \tag{39}$$

where $\mathcal{C}_{\text{photo}} = \beta\kappa I(t)$, and similarly for $\partial \hat{\mathsf{u}}_2/\partial t$.

In the formulation outlined above, there is no axial growth component, i.e. $\dot{\gamma} = 0$, since the integral of A over each cross-section is zero due to the form of A_{tip}. We may naturally incorporate axial growth by adding source and sink terms, as appeared in the gravitropism case. That is, consider the transport equation

$$\frac{\partial A}{\partial t} - \frac{\partial}{\partial s}\left(UA\right) = -QA + C_{\text{in}}\delta(r - r_0) - C_{\text{out}}\delta(x_1)\delta(x_2). \tag{40}$$

Denoting the combined source and sink terms by ΔC, then if this term is independent of s the solution is

$$A(x_1, x_2, s, t) = \left[A_{\text{tip}}\left(x_1, x_2, t - \frac{\ell - s}{U}\right) - \frac{\Delta C}{Q}\right]\exp\left(-\frac{Q(\ell - s)}{U}\right) + \frac{\Delta C}{Q}. \tag{41}$$

In this case, the curvature evolution laws are unchanged, while the axial growth satisfies

$$\frac{\partial \gamma}{\partial t} = \beta\left[\exp\left(-\frac{Q(\ell - s)}{U}\right)\left(\frac{\Delta C}{Q} - 1\right) - A^*\right]. \tag{42}$$

This formulation naturally produces growth focused at the tip, with growing region depending on the turnover. In cases of high turnover, it may be necessary to modify the growth law to avoid 'negative growth' ($\partial \gamma/\partial t < 0$).

D. Circumnutation. In the case of circumnutation, we assume the existence of an axial flow of auxin from a source point. The only difference here is that the auxin gradient originating at the source has a rotational component in the cross section. In the general case, we assume that an internal oscillator produces a time-varying auxin gradient at the point $s = s_c$, i.e.

$$A(s_c, x_1, x_2, t) = \kappa(\cos\theta\, x_1 + \sin\theta\, x_2),$$

where $\kappa = \kappa(t)$ gives the size of the gradient and $\theta = \theta(t)$ describes the orientation in the cross-section. This oscillating gradient provides a simple auxin-level description of the complex mechanisms generating the internal oscillator that are only beginning to be understood (11). The derivation of curvature evolution

is the same as in the phototropism case, simply with $\mathbf{e}_1(t)$ replaced by $\cos(\theta(t))$ and $\mathbf{e}_2(t)$ replaced by $\sin(\theta(t))$. Following the same steps, we obtain the curvature evolution laws

$$\frac{\partial \hat{u}_1}{\partial t} = \mathcal{C}_{\text{circ}} \sin \left(\theta \left(t - \frac{|s - s_c|}{U} \right) \right) e^{-\frac{Q}{U}|s - s_c|}, \qquad [43]$$

$$\frac{\partial \hat{u}_2}{\partial t} = -\mathcal{C}_{\text{circ}} \cos \left(\theta \left(t - \frac{|s - s_c|}{U} \right) \right) e^{-\frac{Q}{U}|s - s_c|}. \qquad [44]$$

where $\mathcal{C}_{\text{circ}} = \beta\kappa$. Note that the model provided in the main text corresponds to the particular choice of a constant rotation rate for the oscillator, $\theta = \omega t$.

E. Thigmotropism. For thigmotropism, we assume that physical contact occurs at a point s_c, and with angle in the local basis ψ_c; that is, the point in physical space

$$\mathbf{r}(s_c, t) + R(\cos \psi_c \, \mathbf{d}_1(s_c, t) + \sin \psi_c \, \mathbf{d}_2(s_c, t)),$$

where R is the cross-sectional radius. Geometrically, generating the helical shape of a twining plant requires establishing a growth gradient which rotates along the axis of the plant with increasing arc length (12). In terms of auxin transport, it has been observed that point contact creates a sharp rise in asymmetric auxin concentration at the stimulus point that is transported along the stem (13, 14). This suggests that we impose as a boundary condition at the contact point an auxin gradient, with minimum auxin at the contact point, i.e.

$$A(x_1, x_2, s_c, t) = -\kappa(\cos \psi_c \, x_1 + \sin \psi_c \, x_2), \qquad [45]$$

where κ characterizes the strength of the tropic response (which may, for instance, be connected to the magnitude of the contact force).

We then assume that auxin flux consists of a rotational cross-sectional component with angular velocity ω, and an axial component with velocity U, thus generating a helical auxin gradient along the stem. The angular component may be seen as a proxy for (largely unknown) underlying mechanisms that generate the rotational component of growth gradient needed for helical twining. For instance, in nutating roots, a circumferential wave of ion flux is engaged; ion fluxes may interact with auxin (15), and also appear sensitive to touch (11), thus providing a possible mechanism.

Following these assumptions, the auxin transport equation is thus

$$\frac{\partial A}{\partial t} + \text{sign}(s - s_c)\frac{\partial}{\partial s}(UA) + \nabla \cdot (Ar\omega\mathbf{e}_\theta) = -QA. \qquad [46]$$

Here the sign function accounts for the flow away from the contact point in either direction, the divergence $\nabla \cdot ()$ is only with respect to the cross-sectional variables, r is the radial position vector within a cross section, and $\mathbf{e}_\theta$ is the circumferential unit vector in the cross section. Since the curvature response is largely localized to the region near the contact point, we neglect any time delay that would occur due to axial transport, and thus consider the steady-state auxin concentration. Setting $\partial A / \partial t = 0$, the exact solution is given by

$$A = -\kappa \left[\cos \left(\psi_c + \frac{\omega}{U}\text{sign}(s - s_c) \right) x_1 + \sin \left(\psi_c + \frac{\omega}{U}\text{sign}(s - s_c) \right) x_2 \right] e^{-\frac{Q}{U}|s - s_c|}. \qquad [47]$$

From here, the evolution equations for $\hat{u}_i$ follow naturally from Eq. (19), by multiplying by x_i and integrating over a cross section, again with the use of Eq. (14).

F. Multiple signals. We model multiple simultaneous signals as an additive effect to the growth response. In particular, consider two stimuli A and B. Letting the auxin concentration under stimulus A be denoted A_A, and similarly A_B for stimulus B, the axial growth law is adapted to

$$\frac{\partial g}{\partial t} = \beta(A_A + A_B - A^*). \qquad [48]$$

An alternative approach would be to formulate a single transport equation with combined flux and/or boundary conditions for each stimulus; however, this would likely negate the mathematical techniques by which we have obtained explicit curvature and growth evolution laws and thus necessitate a fully computational approach. The assumption of separated auxin flows for each stimulus, as utilized here, reflects the differing signal transduction pathways that exist for different stimuli, and leads to an additive growth response, as has been observed to hold reasonably well in the case of photogravitropism (16, 17). In this way, if tropisms A and B lead to the individual curvature laws

$$\frac{\partial \hat{u}_i}{\partial t} = f_A^{(i)}, \quad \frac{\partial \hat{u}_i}{\partial t} = f_B^{(i)}, \ i = 1, 2 \tag{49}$$

respectively, then the curvature evolution under the combined influence of signals A and B is simply

$$\frac{\partial \hat{u}_i}{\partial t} = f_A^{(i)} + f_B^{(i)}. \tag{50}$$

It is also worth noting that different tropisms may act via different hormones, and that auxin affects multiple hormonal pathways (18), potentially acting on different cells within a cross section. In this way, competition between different tropic responses could appear at the level of the cross-sectional growth field g even within a single auxin field.

5. Gravitropism metrics

The metrics used in quantifying the gravitropic response with a rotating base are defined as follows:

1. **Alignment** $= \frac{1}{L} \int_0^L \left(\mathbf{d}_3(S) \cdot \mathbf{e}_z \right)^2 \, \mathrm{d}S$, with $\mathbf{e}_z = (0, 0, 1)$

2. **Curvature** $= \frac{1}{L} \int_0^L \sqrt{u_1^2(S) + u_2^2(S)} \, \mathrm{d}S$

3. **Torsion** $= \frac{1}{L} \int_0^L \left(\frac{u_2'(S)u_1(S) - u_1'(S)u_2(S)}{u_1^2(S) + u_2^2(S)} \right)^2 \, \mathrm{d}S$

The formulas for curvature and torsion follow from Section 1.

6. Escape from the shade - mechanical contact

In simulating the escape from the shade in photogravitropism (main text Fig. 7), contact with the rigid, shade-creating obstacle becomes an issue. Contact at a point $s = s_c$ induces a contact force $\mathbf{f}_c$ that must be accounted for. We assume that the plant may slide along the surface without friction, so that the contact force acts only in the normal direction. Working in a planar geometry with tangent $\mathbf{d}_3$ and transverse direction $\mathbf{d}_1$, this may be expressed as $\mathbf{f}_c = f_c \mathbf{d}_1$. The balance of linear momentum is then

$$\mathbf{n}'(s) = \rho g \mathbf{e}_y + f_c \mathbf{d}_1 \delta(s - s_c). \tag{51}$$

Here we have included self-weight with gravity g acting in the negative $\mathbf{e}_y$ direction and linear density ρ. The delta function $\delta(s - s_c)$ accounts for contact at a single point, and creates a jump in the resultant force $\mathbf{n}$. Both f_c and s_c are unknown values that must be determined at each point in the evolution as part of the solution to the boundary value problem. To determine the two additional unknowns, the system requires two additional conditions, which are that the point $\mathbf{r}(s_c(t), t) = \mathbf{p}$, where $\mathbf{p}$ is the fixed contact point of the obstacle, and we highlight that the contact location along the rod may change with time (since the motion is restricted to a plane, this vector equation consists of the required two scalar conditions).

In simulating this problem, we first integrate the system without contact, monitoring whether any point is near the obstacle, and stopping once a point along the rod first reaches the obstacle, i.e the first time $t = t^*$ at which there exists an $s = s^*$ for which $\mathbf{r}(s^*, t^*) = \mathbf{p}$. At this point, Eq. (51) has a solution with $f_c = 0, s_c = s^*$. For $t > t^*$, we then integrate the system with force balance (Eq. (51)). As a numerical

shooting procedure, we integrate from $s = 0$ to $s = \ell$, in which case the other unknowns are the moment $\mathbf{m} = m\mathbf{e}_z$ and the force components $\mathbf{n} = n_x\mathbf{e}_x + n_y\mathbf{e}_y$ at $s = 0$. The 5 conditions to determine the shooting variables consist of the contact condition $\mathbf{r}(s_c(t), t) = \mathbf{p}$, and the three conditions that make up the free end boundary condition $\mathbf{m} = \mathbf{n} = \mathbf{0}$ at $s = \ell$. In this way, we employ standard continuation techniques to increment the system beyond t^*.

7. Comparison with kinematic models

In this section we demonstrate under which limits and assumptions the curvature evolution laws we have derived correspond with existing kinematic descriptions in the literature.

A. Gravitropism. As noted in the main text, the gravitropism model immediately reduces to the classic 'sine law of gravitropism' (19, 20) when the deformation is restricted to a plane, and generalizes this model for 3D deformations. Furthermore, if the autotropism term is included in the growth law Eq. (21), we recover in the planar case the widely used "graviproprioceptive' model, which is a modified sine law that includes autotropism (21). Both the sine law and the graviproprioceptive model have been validated against experiments involving different plant species (with the conclusion that the latter generally provides a more accurate description (21)).

B. Phototropism. In the case of phototropism, we compare our formulation with the kinematic description of (17) which includes the combined influences of gravitropism, phototropism, and autotropism. In the case when photoception is apical, they posit the curvature evolution equation

$$\frac{\partial C}{\partial t} = -\nu(A(L, t) - A_p) - \beta A - \gamma C, \qquad [52]$$

wehere they use $C(s, t)$ to denote the plant curvature (considering only planar deformations), A_p is the angle the light source makes with the vertical, and the sensitivity to phototropism, gravitropism, and autotropism are respectively described by the parameters ν, β, and γ. Focusing only on the phototropic response, as in our framework the curvature at each point along the stem updates based on the orientation of the tip with respect to the light source; note that in this description the signal is assumed to propagate instantaneously so that at each point along the stem it is the orientation of the tip at the *current* time that dictates the curvature change.

Comparing with our evolution equation Eq. (39), we recover Eq. (52) (with $\beta = \gamma = 0$) under the following assumptions: (i) the deformation is planar so that bending only occurs about the $\mathbf{d}_1$ axis, (ii) the light is assumed to be a plane wave making angle A_p with the vertical (as opposed to a point source in our formulation), (iii) the angle between light source and the tangent $\mathbf{d}_3$ at the tip is small, and (iv) in the limit of $U \to \infty$.

Regarding conditions (ii) and (iii), note that for a planar deformation the tip orientation can be described by the angle α between the vertical and the tangent, so that $\mathbf{d}_3 = (\sin\alpha, \cos\alpha, 0)$, and we have $\mathbf{d}_2 = (-\cos\alpha, \sin\alpha, 0)$. Following the description above, the unit vector pointing towards the light source is given by $\mathbf{e} = (\sin(A_p), \cos(A_p), 0)$. We thus obtain

$$\mathbf{e}_2 = \mathbf{e} \cdot \mathbf{d}_2 = \sin(\alpha - A_p) \approx \alpha - A_p.$$

Plugging this form into Eq. (39) under the limit $U \to \infty$ thus reads

$$\frac{\partial \hat{u}_1}{\partial t} = -\mathcal{C}_{\text{photo}}(\alpha - A_p),$$

which is identical to the phototropism version of Eq. (52) under the substitution $\hat{u}_1 = C$.

C. Nutation. For the problem of nutation, we compare with the recent kinematic description of (22). While the notations and mathematical descriptions significantly differ from our work, the conceptual idea is similar. Namely, the time varying nutational curvature is developed due to an internal oscillator that creates a time varying growth axis and growth differential. In the notation of (22), the growth axis is given by prescribing a function $\psi_g(s,t)$, which is the angle in each cross-section of the growth axis, while the degree of curvature-inducing differential growth is dictated by prescribing a function $\Delta(\psi_g)\dot{E}$. While the kinematic description is outlined for generic forms, in practice the authors assume that ψ_g and $\Delta(\psi_g)\dot{E}$ are only functions of time, i.e. at each time the differential growth field is the same along the length of the plant. They then consider tip patterns in terms of these functions, and demonstrate that circular motion, elliptical motion, and more complex motion can all be obtained. These patterns are in good agreement with experimental observations.

In our notation, the internal oscillator is given by a time-varying auxin source at a single point (typically the tip), and the orientation and degree of differential growth at each point along the length arises as a result of the axial transport of auxin from the tip. In particular, recall that we impose a form of auxin at the tip

$$A_{\text{tip}} = \kappa(\cos\theta\, x_1 + \sin\theta\, x_2),$$

where $\theta = \theta(t)$ gives the orientation of the auxin gradient due to the internal oscillator, playing an equivalent role to the function $\psi_g(t)$ in (22), and the degree of growth differential is determined both by the the the auxin tip gradient κ, which may be taken to be a function of time in general, as well as the sensitivity parameter β in the growth law Eq. (18).

While the transport velocity U and turnover Q of auxin will generate a non-uniform growth response in our framework, we recover the kinematic description of (22) in the limit $U \to \infty$.

8. Parameters and details of simulations

In this section we provide the parameter choices and other relevant details for each of the simulations appearing in the main text and/or supplementary movies. Note that in most cases, we do not consider specific plants, but rather seek to demonstrate the qualitative behavior of the system in different parameter regimes. Thus, we are not concerned here with specific dimensional values, since it is the ratio of different dimensional parameters that dictates the qualitative behavior. Therefore, where possible we have scaled parameters to unity, e.g. the initial rod length can always be taken to equal 1, while varying parameters that enable to explore the qualitative regimes. This choice is not restrictive and amounts to measure all distances with respect to this unit length.

A. Computational details. The models that we have derived are quite simple from a computational perspective as they only involve integration along the arc length. Hence they are all formulated as boundary value problems for ordinary differential equations. Therefore, these equations do not require a dedicated code and, in each scenario, the resulting rod evolution equations were simply solved using *NDSolve* in *Mathematica* (23). In the absence of self-weight or other forces, this is a trivial matter: in such cases $\mathbf{n} = \mathbf{m} = \mathbf{0}$ and the curvature $\mathbf{u}$ is equal to the intrinsic curvature $\hat{\mathbf{u}}$, thus Eqs. (3) and (4) may simply be integrated forward from the clamped base at each time step, and then the intrinsic curvature $\hat{\mathbf{u}}$ is updated quasi-statically.

In cases that include self-weight or other forces, the rod equations at each time step were solved via a numerical shooting method implemented within *NDSolve*. The full system of Eqs. (3), (4) and (8)–(10) is solved by imposing the boundary conditions Eq. (12) at the base, and integrating to the tip with shooting variables $\mathbf{m}(0)$ and $\mathbf{n}(0)$ chosen to match the tip boundary conditions Eq. (13). The shooting variables at one time step form a sufficient guess for the next step, after the intrinsic curvature is updated quasi-statically, and convergence to a solution is rapid so that total simulation time is on the order of seconds. Mathematical notebooks are available in the online Supplementary material with sample code for simulating each of the tropic scenarios modeled.

B. Gravitropism: rotating base. In simulating the rotating base under gravitropism (Fig. 4 main text), we orient the base at angle ϕ_0 from the vertical $\mathbf{e}_z$ direction (note that in terms of the angle θ appearing schematically in Fig. 3(A) of the main text, we have $\theta = \pi/2 - \phi_0$). Expressed in terms of the spherical unit vectors $\mathbf{e}_r = (\sin\phi_0, 0, \cos\phi_0)$, $\mathbf{e}_\phi = (\cos\phi_0, 0, -\sin\phi_0)$, $\mathbf{e}_\theta = (0, 1, 0)$, the frame at the point $S = 0$ is then given the form

$$\mathbf{d}_3(0, t) = \mathbf{e}_r \tag{53}$$

$$\mathbf{d}_1(0, t) = \cos(2\pi\omega t)\mathbf{e}_\phi + \sin(2\pi\omega t)\mathbf{e}_\theta \tag{54}$$

$$\mathbf{d}_2(0, t) = -\sin(2\pi\omega t)\mathbf{e}_\phi + \cos(2\pi\omega t)\mathbf{e}_\theta. \tag{55}$$

We fix $\omega = 1$, which is equivalent to scaling time based on the rotation rate of the base. We also set $\phi_0 = \pi/3$ and scale the total length $L = 1$. We simulate the gravitropic curvature laws with no axial growth and response rate $\mathcal{C}_{\mathrm{grav}}$ taking values of $\mathcal{C}_{\mathrm{grav}} = \{0.1, 1, 10, 50\}$. In this simulation we ignore the effect of self-weight, so that mechanical equilibrium is automatically satisfied with $\mathbf{u} = \hat{\mathbf{u}}$; we thus integrate Eqs. (3) and (4) to determine the morphology at each time step, and then update the curvature. Each parameter set is simulated up to time $t = 3$, which corresponds to three complete rotations of the base.

C. Phototropism.

Fixed light source. In simulating planar phototropism for a fixed light source (Fig. 5 of the main text), a light source is placed at the point $(1, 1)$, and the parameters $\ell = 1$, $U = 1$, and $\gamma \equiv 1$ (no axial growth) are fixed. This is equivalent to scaling time based on axial transport. The plant is clamped at the origin with tangent $\mathbf{d}_3 = (0, 1)$ at $s = 0$. We then simulate up to $t = 10$ for each combination of the parameter choices $Q = \{1, 5\}$, $\mathcal{C}_{\mathrm{photo}} = \{0.5, 2.5\}$, to represent the different regimes of high and low turnover and phototropic response, respectively.

Note also that in simulating the time-delay differential equations, it is necessary to provide the form of the functions $\mathbf{e}_i$, $i = 1, 2$ for $-\ell/U \leq t < 0$. These are chosen to be constant and equal to the value at $t = 0$, determined by the initial orientation.

Moving light source - day/night cycle. To simulate a day/night cycle (Fig. 6 of main text), we set $U = 1$, $\ell = 1$, $Q = 0.1$, $\gamma \equiv 1$, and $\mathcal{C}_{\mathrm{photo}} = 1.5$. A light source with intensity $I(t) = \max\{0, \sin\omega t\}$ follows the path $\mathbf{p}(t) = (R\cos\omega t, Y, R\sin\omega t)$, where $\omega = 0.2$, $R = 3$, and $Y = 2$.

In the case of the additional autotropism terms, we increase $\mathcal{C}_{\mathrm{photo}}$ to 3 and set $\xi = 0.3$. The increase in $\mathcal{C}_{\mathrm{photo}}$ is chosen so that the motion during the day is similar to the non-autotropic case, as the autotropism serves to diminish the phototropic response in the presence of a stimulus. In both cases, one complete period is simulated, corresponding to day – when $I(t) > 0$, and night – when $I(t) = 0$.

D. Photogravitropism.

Fixed light source. For the simulations of main text Fig. 7 (A)-(E), we fix the parameters $U = 1$, $Q = 0.1$ and $\mathcal{C}_{\mathrm{photo}} = 1$. Growth is uniform and linear: $\gamma = 1 + ct$ with $c = 0.1$, and initial length $L = 1$. A light source is placed at the point $\mathbf{p} = (4, 1)$. The plant is clamped at the origin with tangent $\mathbf{d}_3 = (0, 1)$ at $s = 0$. We then simulate up to $t = 10$ for each combination of the parameter choices $G = \{0.25, 2.5\}$, $\mathcal{C}_{\mathrm{grav}} = \{0.1, 1\}$, . Here the parameter G characterizes the effective impact of self-weight under gravity. In particular, by scaling rod length by L, moment by E_b/L where E_b is the bending stiffness, and noting that the gravitational force has magnitude ρg, the non-dimensional moment balance equation, expressed in the reference variable S, is

$$m'(S) = -\gamma^2 G(S - 1)\cos(\theta(S)), \quad G := \frac{\rho g L^3}{E_b} \tag{56}$$

where θ is the angle between the tangent and the x-axis. In obtaining Eq. (56) we have used the geometric expression $\mathbf{r}'(S, t) = \gamma\mathbf{d}_3 = \gamma(\cos\theta\mathbf{e}_x + \sin\theta\mathbf{e}_y)$, and that the solution to the force balance $\mathbf{n}'(S) = \gamma\rho g\mathbf{e}_y$ subject to $\mathbf{n} = \mathbf{0}$ at $S = L$ is $\mathbf{n} = \rho g(S - L)\mathbf{e}_y$.

Thus, the parameter choices for G and $\mathcal{C}_{\text{grav}}$ represent the different regimes of high and low mass/gravity and gravitropic response, respectively.

Canopy escape. In simulating the escape from shade (Fig. 7 (D)-(E) in main text), we have set $U = 1$, $Q = 0.5$, $\mathcal{C}_{\text{photo}} = 1$, $\mathcal{C}_{\text{grav}} = 0.1$, $\gamma = 1 + 0.25t$, $G = 0.05$ (see parameter description above). The initial length is $L = 1$, and the plant is clamped at the origin with tangent $\mathbf{d}_3 = (0, 1)$ at $s = 0$. The shade creating obstacle occupies the region (x, y) with $x \leq 1$, $y \geq 1.2$, so that the corner point and eventual contact point is $\mathbf{p} = (1, 1.2)$.

E. Circumnutation. For the simulations of circumnutation, main text Fig. 8 (A)-(B), the internal oscillator is located at the tip, with angular velocity $\omega = 1$; thus the period is 2π and we simulate one complete period. Plant length is scaled to $L = 1$, and axial growth is turned off ($\gamma \equiv 1$). In Fig. 8 (A) other parameters are $U = 5$, $Q = 5$, $\mathcal{C}_{\text{circ}} = 2$; in Fig. 8 (B) we use $U = 5$, $\mathcal{C}_{\text{circ}} = 1$, and we vary the turnover: $Q \in \{1, 2, 3 \ldots, 10\}$. In Fig. 8 (C) the parameters are $U = 5$, $Q = 5$, $\mathcal{C}_{\text{circ}} = 1$, and the angular velocity is non-uniform; in particular the auxin gradient at the tip follows the line

$$\cos\theta x_1 + \sin\theta x_2,$$

with

$$\theta(t) = \omega t + \alpha \sin \hat{\omega} t.$$

The tip profiles in the figure are plotted for $\omega = 1$, $\hat{\omega} = 5$, and varying $\alpha = \{0, 0.15, 0.3, \ldots, 1.5\}$.

In these simulations we have also given the plant an initial curvature, which serves to better center the motion about the base of the plant, for visualization purposes (the initial curvature only creates a translation of the tip pattern). The initial curvatures used were as follows: $\mathsf{u}_1 = 0$ in Fig. 8 (A)-(C), while $\mathsf{u}_2 = 1.25$ in Fig. 8 (A), $\mathsf{u}_2 = 0.5$ in Fig. 8 (B), and $\mathsf{u}_2 = 0.45 - 0.07\alpha$ in Fig. 8 (C) (this choice was made to avoid overlapping of the tip patterns with varying α).

F. Thigmotropism. In simulating thigmotropism, main text Fig. 8 (D)-(F), we have set $\mathcal{C}_{\text{thig}} = 10$, and varied the turnover Q and angular velocity ω as follows: $Q = 3, \omega = 2$ in Fig. 8 (D), $Q = 3, \omega = 6$ in Fig. 8 (E), and $Q = 5, \omega = 6$ in Fig. 8 (F). Again, axial growth is turned off and the plant length is $L = 1$. In each case total simulation time is $t = 10$. In the thigmotropism formulation, with the signal coming from a single point, the curvatures may be determined exactly, given by

$$\mathsf{u}_1 = -\mathcal{C}_{\text{thig}} \exp\left(-\frac{QS}{U}\right) \sin\left(\psi_0 + \frac{\omega S}{U}\right) t, \tag{57}$$

$$\mathsf{u}_2 = \mathcal{C}_{\text{thig}} \exp\left(-\frac{QS}{U}\right) \cos\left(\psi_0 + \frac{\omega S}{U}\right) t. \tag{58}$$

Here the angle ψ_0 indicates the point of contact (which is set at $s = 0$). In the presented simulations, $\psi_0 = \pi/2$, so that the contact point is at $\mathbf{r}(0, t) + a\mathbf{d}_2$, where a is the cross-sectional radius, which was fixed at $a = 0.02$. From the formulas in Section 1, we then obtain that the curvature κ and torsion τ will evolve according to

$$\kappa = \mathcal{C}_{\text{thig}} \exp\left(-\frac{QS}{U}\right) t \tag{59}$$

$$\tau = \frac{\omega}{U}. \tag{60}$$

Note that a helix of radius α and pitch β (i.e. where the angle of the helix ϕ satisfies $\tan\phi = \beta/\alpha$) has curvature $\hat{\kappa} = \alpha/\left(\alpha^2 + \beta^2\right)$ and torsion $\hat{\tau} = \beta/\left(\alpha^2 + \beta^2\right)$. Since the torsion of the plant is fixed by the ratio of rotational to axial auxin velocity, Eq. (60), and the helical radius for a pole of radius c and plant radius a is $\alpha = c + a$, we can solve for the pitch, or equivalently the angle ϕ, which satisfies $\sin(2\phi) = \omega(a + c)/U$. It follows that the curvature $\hat{\kappa} = \cos^2\phi/(a + c)$; in our simulations we have fixed the pole radius $c = 0.05$.

In this formulation, the curvature increases linearly in time at every point. This unrealistic (in long times) aspect could be corrected by having a depleting auxin source at the contact point. However, in any case we must account for the fact that the curvature cannot increase beyond $\hat{\kappa}$, simply due to the presence of the pole. Thus, in simulating the wrapping around a pole, at each spatial point we increase the curvatures according to Eqs. (57) and (58), until the curvature $\kappa = \hat{\kappa}$, where κ is given by Eq. (59), at which point we freeze the curvatures in the simulation (in this way, we account for the fact that the intrinsic curvature may keep increasing, but the actual curvature may not due to the mechanical contact, while avoiding the problem of having to compute the mechanical contact force density).

G. Pole dance. In SI movies, we include a simulation that consists of a plant that searches for a pole via the circumnutation model, while also undergoing axial growth, and then begins to wrap around it following the thigmotropism model once contact is made. In this simulation, the parameters used were $U = 6$, $Q = 10$, $\mathcal{C}_{\text{circ}} = 3$, and circumnutation oscillator frequency $\omega = 5$ originating at the base $S = 0$. The plant is clamped at the origin, has radius $a = 0.025$, is initially straight and has initial length $L = 1$ and growth rate $\partial\gamma/\partial t = 0.4$. A vertical pole with radius $c = 0.05$ passes through the point $\{-0.68, -0.52, 0\}$. The plant first makes contact with the pole at time $t = 3$, and at contact point defined by reference arc length $S_c = 0.8$ and angle $\psi_c = 2.26$ (note that rather than defining the location of the pole, we have defined the location and time of the contact, and used these to define the pole; we then verify that with the pole defined in this way, no prior contact was made).

Once contact is made, we turn off the circumnutation signal, and only evolve the portion of the plant, $S > S_c$, i.e. from pole to end. This follows the thigmotropism curvature evolution, with parameters $U = 1$, $Q = 3$, $\mathcal{C}_{\text{thig}} = 9$, and $\omega = 0.77$. The choice of ω is made for computational convenience, as this particular value means that the pitch of the helix is exactly equal to the angle at which contact is made, and no rotation of the tangent about the contact point is needed. The wrapping portion of the evolution is simulated from $t = 3$ up to $t = 4.5$.

9. Comparison to experiment

Section 3 of the main text includes model comparison with 3 distinct tropic experiments, with results plotted in main text Fig. 9. Below we outline experimental and model comparison details. The objective in this analysis was to demonstrate the general validity of the modeling framework, as opposed to a detailed analysis of any given experiment; therefore model parameter choices were chosen by direct comparison with the data. We have maintained parameter consistency across different setups of the same experiment, e.g. the gravitropism sensitivity is not changed when phototropic effects are added.

A. Fig. 9(A). for this subfigure we consider the data in Fig. 1A of (24). In this set of experiments the hypocotyls of cucumber plants were subjected to gravistimulation and thigmotropism, with the resultant bending response measured over a period of 24 hours. In the control experiment, plotted as the red data points in our main text Fig. 9(A), the plants were placed in a horizontal position; the increase in curvature measures the bending towards the vertical as a gravitropic response. The blue data points correspond to an experimental setup with the plants situated vertically and given an asymmetric mechanical perturbation at the start of the experiment. This caused the plants to bend horizontally toward the direction of the stimulus, but since the stimulus did not persist they then reorient to the vertical under gravitropism; hence the increase and subsequent decrease in curvature. These are shown schematically in SI Fig. 1. In simulating these experiments, we employed a combination of gravitropism, thigmotropism, and autotropism. Note that while the authors do not specifically mention autotropism, its inclusion has been found to match gravitropic data more accurately than gravitropism alone (21); we found this to be the case as well. In the experiments, the mechanical perturbation is applied not a single point but rather by rubbing a needle along the entire length of the hypocotyl. To account for this in our model of the thigmotropic response, we make 3 assumptions:
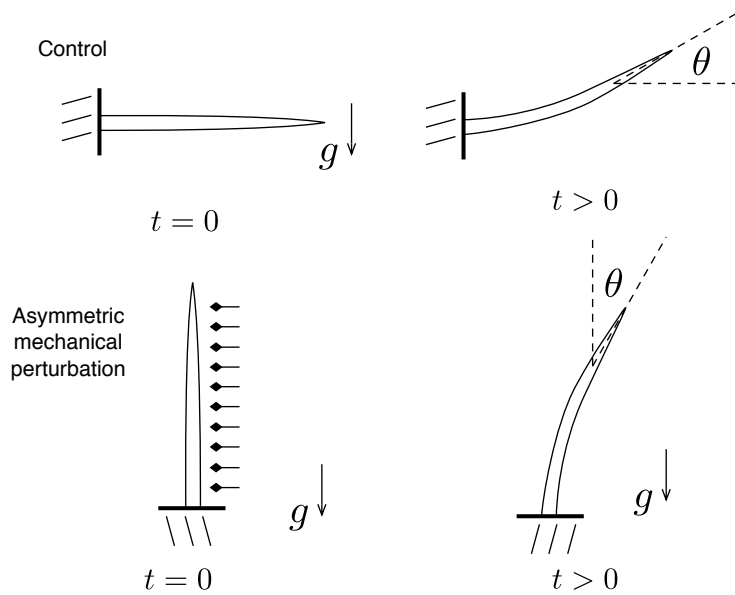
Fig. 1. Schematic for the experiments of (24) and model comparison.

517   1. The uniformly applied signal generates a spatially independent response.

518   2. The signal provided at $t = 0$ decays exponentially with rate β.

519   3. We restrict our attention to 2D deformation, i.e. we do not allow torsion to develop.

520 With regards to point 3, the images in Fig. 3 of (24) do suggest some degree of torsion, consistent with our
521 model, however the sections are too short for significant torsion to develop or be measured, and moreover
522 only a single curvature measure is available for the data we plot. In terms of Eqs. (57) and (58), this is
523 equivalent to setting the angular component ω to zero. This generates a planar deformation, for which
524 $\mathsf{u}_1 = 0$, while u_2 satisfies

$$\frac{\partial \mathsf{u}_2}{\partial t} = \mathcal{C}_{\mathrm{grav}} \cos \theta(S) - \mathcal{C}_{\mathrm{thig}} \exp(-\beta t) - \xi \mathsf{u}_2, \tag{61}$$

526 where θ is the angle between the tangent and the horizontal axis (note gravity is oriented vertically downward
527 as shown in Fig. 1. To simulate the control experiment, the $S = 0$ end is clamped at $\theta = 0$; for the
528 thigmotropic experiment the $S = 0$ end is clamped at $\theta = \pi/2$. Both scenarios were run for total time
529 $t = 24$ hr in correspondence with the data, and the total length is estimated to be 5 cm. The continuous
530 curves shown in main text Fig. 9 correspond to the angle θ measured at the tip for the parameter choices:
531 $\mathcal{C}_{\mathrm{grav}} = 0.033$ (cm.hr)$^{-1}$, $\xi = 0.11$ hr^{-1}, $\mathcal{C}_{\mathrm{thig}} = 0.033$ (cm.hr)$^{-1}$ (and $\mathcal{C}_{\mathrm{thig}} = 0$ for control), and $\beta = 0.13$
532 hr^{-1}.

533 **B. Fig. 9(B).** This subfigure includes the circumnutation patterns appearing in Figs 3 and 4 (11) (see also
534 references therein for the initial studies noted in this review paper), corresponding to tip patterns measured
535 in three-week old sunflower plants.

536   In simulating these we aim to reproduce the diversity of patterns, which can roughly be described
537 as circular, elliptical, and rosette-like. We consider both circumnutation and circumnutation combined
538 with gravitropism. The simulations follow Eq. (43) in the case of circumnutation only, and with the
539 additional gravitropism terms corresponding to the right-hand sides of Eqs. (33) and (34) in the combined
540 circumnutation and gravitropism. For circumnutation, the auxin source and internal oscillator are located
541 at the tip $s_c = 1$, with transport parameters $U = 15$ and $Q = 5$. The gravitropism response is $\mathcal{C}_{\mathrm{grav}} = 0.5$.
542 The internal oscillator is given by
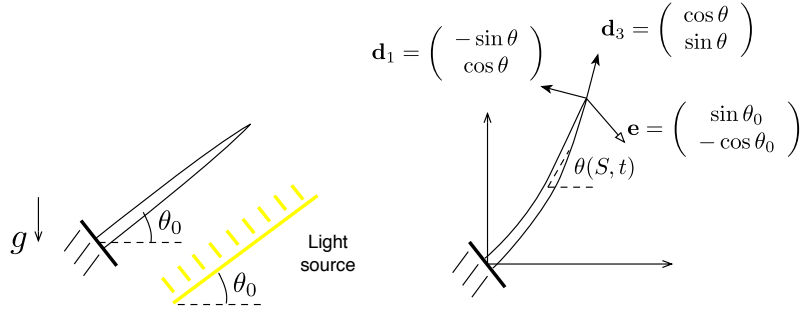
Fig. 2. Schematic for the experiments of (25) and model comparison.

543   1. circle (left-most plot of main text Fig. 9(B)): $\theta(t) = t$

544   2. ellipse (middle plot of main text Fig. 9(B)): $\theta(t) = t - 0.5\sin(2t)$

545   3. rosette (right-most plot of main text Fig. 9(B)): $\theta(t) = t - 0.5\sin(1.7t)$

546 Note the small difference in θ between the elliptical and rosette-like cases, demonstrating how a small
547 change in the rate of internal oscillator can produce significantly distinct patterns.
548   In each case, we simulate the motion for a total time $t = 6\pi$. As the experimental rosette pattern
549 demonstrates a spiraling out as time increases, here we have included a small axial growth component, with
550 growth stretch γ satisfying $\dot{\gamma} = 0.02$. For visual purposes, a constant initial curvature u_2 was given at time
551 $t = 0$ in order to center the tip pattern around the origin. This took the value $\mathsf{u}_2 = 0.3$ for the rosette and
552 ellipse, and $t = 0$ in order to center the tip pattern around the origin. This took the value $\mathsf{u}_2 = 0.4$ for the
553 circle.

C. Fig. 9(C). This subfigure includes data from Fig. 4 of (25). In these experiments, a young poplar stem is
given a gravitropic stimulus by titling of the base, and is then subjected to either an isotropic or anisotropic
light stimulus. The shape of the stem was recorded at different time points, providing x and y coordinates
for digitized points along the stem. This data was extracted for select time points (note that we are not
showing the shape at all time points, but rather a representative sample spanning the full time-scale of the
experiment). using WebPlotDigitizer, and appears as the symbols in main text Fig. 9(C). The left plot
is the data for the isotropic light, the right plot has an anistropic light source generated by neon tubes
located to the right of the plant and oriented at the same angle of tilt (see (25) Fig. 3). To simulate
these experiments, we use a combination of gravitropism, phototropism, and autotropism. In the case of
the isotropic light, since there is no directionality, we treat this case with phototropism omitted. As the
deformation is confined to a plane, the curvature $\mathsf{u}_1 = 0$, while u_2 can be described in terms of the angle
$\theta = \theta(S, t)$ between the tangent and the x-axis. The light is oriented at angle θ_0 from the horizontal, which
is the same as the angle of the base, following (25) Fig. 3. The in-plane tangent vectors then satisfy

$$\mathbf{d}_1 = \begin{pmatrix} -\sin\theta \\ \cos\theta \end{pmatrix}, \quad \mathbf{d}_3 = \begin{pmatrix} \cos\theta \\ \sin\theta \end{pmatrix}$$

The unit vector pointing from the tip towards the light is given by

$$\mathbf{e} = \begin{pmatrix} \sin\theta_0 \\ -\cos\theta_0 \end{pmatrix},$$

from which we obtain

$$\mathsf{e}_1(t) = \mathbf{d}_1(L,t) \cdot \mathbf{e} = -\cos(\theta(L,t) - \theta_0).$$

The curvature evolution law is thus given by

$$\frac{\partial \mathsf{u}_2}{\partial t} = \mathcal{C}_{\text{grav}} \cos \theta - \mathcal{C}_{\text{photo}} \exp\left(-\frac{Q}{U}\gamma(1-S)\right) \mathsf{e}_1\left(t - \frac{\gamma(1-S)}{U}\right) - \xi \mathsf{u}_2, \qquad [62]$$

with e_1 as given above. This is illustrated schematically in SI Fig. 2. The data extracted from (25) shows a significant increase in axial length over the course of the experiments. We incorporate this via a simple uniform axial extension with growth rate c, i.e. we impose $\gamma = 1 + ct$.

For tree saplings, self-weight is probably not negligible, and we have included it as outlined in SI Section D, with the impact of self-weight characterized by the single parameter G as in Eq. 56.

In generating the model predictions, represented by the solid curves in main text Fig. 9(C), we have used simulation parameters $\mathcal{C}_{\text{grav}} = 0.3$, $\xi = 0.1$, $G = 0.3$, $c = 0.06$, and in the right column with phototropism included, we use parameters $\mathcal{C}_{\text{photo}} = 0.11$, $U = 2$, and $Q = 0.75$ (with gravitropic and autotropic parameters unchanged). The data indicate a longer total time represented in the anisotropic phototropism case, so we have simulated these for total time $t = 10$ for the left column and $t = 14$ for the right column.

The time between successive curves in the data is determined by the labels in the legend of (25) Fig. 4. To relate these to the model predictions, we scale the total simulation time to match the difference in the first and last time points displayed in the data, and plot the simulated curves at the corresponding time points for each data curve. Explicitly, the data curves extracted are for the following time points as presented in the legends of (25) Fig. 4:

- left plot (isotropic light): $\{274, 281, 285, 290, 299\}$

- right plot (anisotropic light): $\{172, 176, 180, 193, 201\}$

The data and simulation plots follow these time points, with color changing successively through the set $\{$red, yellow, green, blue, purple$\}$.

10. Description of Movies

SI movie S1: Gravitropism with rotating base, and gravitropic response parameter $C_{\text{thig}} = 0.1$. Other simulation parameters provided in SI Section 7.

SI movie S2: Gravitropism with rotating base, and gravitropic response parameter $C_{\text{thig}} = 1$. Other simulation parameters provided in SI Section 7.

SI movie S3: Gravitropism with rotating base, and gravitropic response parameter $C_{\text{thig}} = 10$. Other simulation parameters provided in SI Section 7.

SI movie S4: Gravitropism with rotating base, and gravitropic response parameter $C_{\text{thig}} = 50$. Other simulation parameters provided in SI Section 7.

SI movie S5: Phototropism, simulation of a day-night cycle, with no autotropism. Simulation parameters provided in SI Section 7.

SI movie S6: Phototropism, simulation of a day-night cycle, with autotropism. Simulation parameters provided in SI Section 7.

SI movie S7: Thigmotropism, pole wrapping, with low turnover ($Q = 3$) and low angular velocity ($\omega = 2$). Other simulation details provided in SI Section 7.

SI movie S8: Thigmotropism, pole wrapping, with low turnover ($Q = 3$) and high angular velocity ($\omega = 6$). Other simulation details provided in SI Section 7.

SI movie S9: Thigmotropism, pole wrapping, with high turnover ($Q = 5$) and low angular velocity ($\omega = 6$). Other simulation details provided in SI Section 7.

SI movie S10: Pole dance. Circumnutation with axial growth, followed by thigmotropic pole wrapping. Simulation parameters provided in SI Section 7.

1. Moulton DE, Lessinnes T, Goriely A (2020) Morphoelastic rods III: Differential growth and curvature generation in elastic filaments. *Journal of the Mechanics and Physics of Solids* 142:104022.
2. Band LR, et al. (2014) Systems analysis of auxin transport in the Arabidopsis root apex. *The Plant Cell* 26(3):862–875.
3. Fozard J, Bennett M, King J, Jensen O (2016) Hybrid vertex-midline modelling of elongated plant organs. *Interface Focus* 6(5):20160043–14.
4. Chauvet H, Moulia B, Legué V, Forterre Y, Pouliquen O (2019) Revealing the hierarchy of processes and time-scales that control the tropic response of shoots to gravi-stimulations. *Journal of experimental botany* 70(6):1955–1967.
5. Mitchison G (2015) The Shape of an Auxin Pulse, and What It Tells Us about the Transport Mechanism. *PLoS Computational Biology* 11(10):e1004487–25.
6. Larsen P (1955) Growth substances in higher plants in *Moderne Methoden der Pflanzenanalyse/Modern Methods of Plant Analysis.* (Springer), pp. 565–625.
7. Band LR, King JR (2011) Multiscale modelling of auxin transport in the plant-root elongation zone. *Journal of mathematical biology* 65(4):743–785.
8. Digby J, Firn R (1995) The gravitropic set-point angle (gsa): the identification of an important developmentally controlled variable governing plant architecture. *Plant, cell & environment* 18(12):1434–1440.
9. Roychoudhry S, Del Bianco M, Kieffer M, Kepinski S (2013) Auxin Controls Gravitropic Setpoint Angle in Higher Plant Lateral Branches. *Current Biology* 23(15):1497–1504.
10. Hohm T, et al. (2014) Plasma membrane h+-atp ase regulation is required for auxin gradient formation preceding phototropic growth. *Molecular systems biology* 10(9):751.
11. Stolarz M (2014) Circumnutation as a visible plant action and reaction. *Plant Signaling & Behavior* 4(5):380–387.
12. Silk WK (1989) On the Curving and Twining of Stems. *Environmental and Experimental Botany* 29(1):95–109.
13. Lee HJ, Kim HS, Park JM, Cho HS, Jeon JH (2020) PIN-mediated polar auxin transport facilitates root–obstacle avoidance. *New phytologist* 225(3):1285–1296.
14. Reinhold L, Sachs T, Vislovska L (1972) The role of auxin in thigmotropism in *Plant Growth Substances 1970.* (Springer), pp. 731–737.
15. Shabala SN, Newman IA (1997) Root nutation modelled by two ion flux-linked growth waves around the root. *Physiologia Plantarum* 101:770–776.
16. Galland P (2002) Tropisms of avena coleoptiles: sine law for gravitropism, exponential law for photogravitropic equilibrium. *Planta* 215(5):779–784.
17. Bastien R, Douady S, Moulia B (2015) A Unified Model of Shoot Tropism in Plants: Photo-, Gravi- and Propio-ception. *PLoS Computational Biology* 11(2):e1004037–30.
18. Semeradova H, Montesinos JC, Benkova E (2020) All roads lead to auxin: Post-translational regulation of auxin transport by multiple hormonal pathways. *Plant Communications* p. 100048.
19. Sachs J (1882) *Vorlesungen über Pflanzen-Physiologie.* (W. Engelmann) Vol. 1.
20. Moulia B, Fournier M (2009) The power and control of gravitropic movements in plants: a biomechanical and systems biology view. *Journal of experimental botany* 60(2):461–486.
21. Bastien R, Bohr T, Moulia B, Douady S (2013) Unifying model of shoot gravitropism reveals proprioception as a central feature of posture control in plants. *PNAS* 110(2):755–760.
22. Bastien R, Meroz Y (2016) The Kinematics of Plant Nutation Reveals a Simple Relation between Curvature and the Orientation of Differential Growth. *PLoS Computational Biology* 12(12):e1005238–20.
23. Wolfram Research, Inc. (2019) Mathematica, Version 12.0. Champaign, IL, 2019.
24. Jaffe MJ, Takahashi H (1990) Thigmotropism and the inodulation of tropistic curvature by mechanical perturbation in cucumber hypocotyls. *Physiologia Plantarum* 80:561–567.
25. Coutand C, Adam B, Ploquin S, Moulia B (2019) A method for the quantification of phototropic and gravitropic sensitivities of plants combining an original experimental device with model-assisted phenotyping: Exploratory test of the method on three hardwood tree species. *PloS one* 14(1):e0209973–28.